International Journal of Heat and Mass Transfer 129 (2019) 415–426

Contents lists available at ScienceDirect

International Journal of Heat and Mass Transfer

journal homepage: www.elsevier.com/locate/ijhmt

Absolute permeability calculations in micro-computed tomography models of sandstones by Navier-Stokes and lattice Boltzmann equations

Timur Zakirov *, Akhmet Galeev

Institute of Geology and Petroleum Technologies, Kazan Federal University, Kremlin str., 18, Kazan 420008, Russia

ARTICLE INFO

Article history:
Received 9 June 2018
Received in revised form 22 September 2018
Accepted 27 September 2018
Available online 4 October 2018

Keywords:
Absolute permeability
Navier-Stokes equations
Lattice Boltzmann equations
X-ray CT images
Porous media

ABSTRACT

This paper investigates the calculation features of sandstones absolute permeability coefficients on their digital images using the lattice Boltzmann equations (LBE) and Navier-Stokes equations (NSE). The main attention in this work is given to comparison of numerical solutions of NSE and LBE, and to study the effects of grid refinement and grid coarsening on the calculated permeability coefficient. 3D digital images of sandstones were obtained using X-ray computed tomography. The permeability coefficients were calculated in sandstone samples from Imperial College London open library as well as from Ashalchinskoe (Tatarstan, Russia) and Vostochno-Birlinskoe (Ulyanovsk region, Russia) oil fields. When using LBE, a multi-relaxation time collision operator was applied. It was shown that permeability coefficients, calculated using LBE, of original digital images are 20–30% higher than when using NSE. The study of grid refinement was performed at the refinement levels ranges from 2 to 10. In this paper, the level of grid refinement characterizes the multiplicity of the grid step splitting. Strong dependence of the permeability coefficients on the grid refinement level was revealed for each mathematical model. The NSE solutions are significantly less sensitive to the refinement level in comparison with LBE solutions and the discrepancy between them decreases with increase in the refinement level. The grid independence of the NSE solution is achieved at grid refinement level 3, whereas for LBE even refinement level 10 is not enough for this. Issues arising from grid coarsening are discussed and solutions are developed at coarsening resolutions in two and three times. It was found that grid coarsened in two times is valid for single-phase flow simulations and for calculation of permeability coefficients with good accuracy of <10% error compared to original grid. This result allows one to reduce the grid dimension in 2^3 times which can significantly economy computational cost. For grid coarsened in three times, the calculated flow characteristics deviate by more than 10% from the initial values, but deviations decrease with increasing permeability.

1. Introduction

The permeability of reservoir rocks is one of the most critical properties measured on core samples in laboratory experiments [1–4]. Experimental modeling of the reservoir conditions in laboratory, along with the need to take into account many textural and geological factors, has a number of objective and inevitable shortcomings: high price and labor costs, long time of experiments on samples with low permeability and/or for high viscosity oils. In the last decade, since the experimental and computed technologies are developing, the numerical simulation of the porous rocks characteristics attracts growing attention. It is based on the use of digital 3D images of porous media, which are extracted by X-ray computed tomography scanning (X-ray CT), and has the generally accepted name "Computational Rock Physics". This approach assumes the successive operations [5]: X-ray CT scanning and reconstruction of 3D digital model; image processing; mathematical modeling of one or more fluids flow in the digital model of pore space and calculation of its properties. The output of the first two stages is a voxelized (voxel is an analog of pixel in 3D space) model of the rock with a given geometry of pore space. Thus, the investigation of flow processes in the pore-scale leads to the hydrodynamic modeling in domain with known arrangement of impermeable boundaries.

The mathematical models which are frequently used by the researchers for single-phase flow studying in pore-scale can be divided into two groups: the stationary Navier-Stokes equations (NSE) and the lattice Boltzmann equations (LBE). Computational

* Corresponding author.
E-mail addresses: tirzakirov@kpfu.ru (T. Zakirov), Akhmet.Galeev@kpfu.ru (A. Galeev).

https://doi.org/10.1016/j.ijheatmasstransfer.2018.09.119
0017-9310/

simulations with the NSE are particularly discussed in [6–10]. In [6], a numerical approximation of the NSE by finite-difference method is considered. A special attention is given to nodes near impermeable boundaries. The properties of sand and carbonate reservoirs, as well as samples with random packing of spherical particles are investigated using NSE in [7–10].

The LBE are based on the principles of statistical fluid mechanics. The theoretical foundations are considered in [11,12]. The LBE are well adapted for numerical simulations in flow domains with large number of impermeable obstacles corresponding to a skeleton due to simple description of boundary conditions (“bounce back” rule) [13]. In [14], the permeability coefficients of samples with random packing of spherical and cubic particles were calculated using LBE. The influence of randomness of the particles packing and their sizes on the permeability coefficients was considered. In [15], a single-phase flow was simulated in the layers of the carbon paper. The correlations between permeability and porosity coefficients were revealed, the effect of the sample compression on the flow properties was also evaluated. The permeability coefficients of carbonate reservoirs were investigated in [16] using LBE. Strong anisotropy of the pore space was revealed. It was found in [7,8,16] that small sizes (2–3 mm) of the carbonate rocks are not representative for upscaling of the porosity and permeability coefficients from micro-scale (few millimeters) to lab-scale (centimeters and more). The comparison of LBE and finite-difference method was carried out in [17]. It was obtained a 6% difference between permeability coefficients calculated using these two methods.

One of the LBE solution stages is the description of particles collision, as a result of which the system tends to the equilibrium state [11]. Depending on the type of collision operator, the Single relaxation time (SRT) [11,18,19] and the Multi relaxation time (MRT) models [19–22] are distinguished. The theoretical foundations of these approaches are also discussed in [23]. During the tests of collision operators on the Couette and the Poiseuille flows, it was shown that the MRT model produces more accurate results in comparison with SRT operator [19,24]. A number of papers examined MRT and SRT operators when studying the flow in a porous medium. In [25], the flow characteristics of the “body centered cube” flow region (BCC) were calculated. A strong influence of the viscosity on permeability coefficients was revealed when using SRT model, whereas for MRT model the dependence is absent. Similar results were also obtained in [26] for “face centered cube” flow domain (FCC), for model with random packing of spherical particles in [18] and for layers of carbon paper in [15].

An alternative approach for the NSE and the LBE is a pore-network model (PNM). In the PNM, the original image of pore space is associated with a model of spherical pores connected by cylindrical capillaries [27,28]. The hydrodynamic modeling in the PNM is based on the law of mass conservation and on the known characteristics of the Poiseuille flow in cylindrical capillaries.

A group of papers [29–31] is devoted to various methods of image processing and segmentation. They demonstrate the significant influence of these procedures on the properties of porous media. The affect of digital model resolution on its characteristics was considered in [23,31–34]. It was revealed that the properties of porous media are very sensitive to detail of the pore space description.

Since digital models are characterized by large grid dimensions (about 300^3–500^3 cells), the investigation of flow processes imposes serious demands on the computer technique and the effectiveness of software algorithms. From the point of computational and time costs, the NSE and the LBE have peculiarities. The LBE describe nonstationary fluid flow. Calculation of the absolute permeability coefficient, as known, is carried out under the steady flow regime which is achieved, on the average, after 10,000–20,000 iterative time steps. For this reason, the time costs when using LBE, at the first glance, exceed stationary NSE. On the other hand, compared with NSE, the LBE are easier adapted for the software algorithms parallelization using GPGPU or OpenMP technologies [35–37]. This is explained by the fact that LBE solution is traditionally performed using an explicit scheme and, therefore, the volume of parallelism is sufficient. The NSE is more complicated for numerical solution. The effective solving of sparse system of linear algebraic equations with large dimension is a special importance problem. Direct methods based on the matrix factorization lose their power with the growth of unknown numbers due to the nonlinear increase in the RAM and the number of operations [38,39]. Thus, iterative methods based on Krylov subspace [40] are the only practical alternative for such calculations. At the same time, the correct choice of a preconditioner which makes it possible to reduce the number of iterations and, accordingly, the computational cost is critically important. The multigrid methods shown in [41] have a good scalability, demonstrate a high rate of the convergence and practically independent of the grid dimension. However, for the NSE, standard multigrid methods often lose their effectiveness and require the applying of special methods. The only possible approach is the use of two-stage preconditioners which separately consider fluid pressure and velocity. This method is implemented in the open source AMGCL library (https://github.com/ddemidov/amgcl, [42]).

The comparison of porous media properties obtained by numerical and experimental methods is well known problem. On the one hand, this problem is related to the difference in sizes of the examined samples. Thus, a correct comparison is possible only for homogeneous samples. In [25], for artificially generated in computer BCC model, a successful comparison between LBE results and the analytical formula, which predicts permeability in that domain, was obtained. The experiments in laboratory conditions are usually carried out for samples which volumes by two and three orders of magnitude exceed the volumes of micro-CT images (a few millimeters). A good agreement between numerical and experimental data was obtained in [16], but the resolution of X-ray CT image was too low (about 45 μm) due to large size of the sample (4.5 cm). On the other hand, the permeability coefficients, estimated by different experimental methods, can have a high scatter up to three orders of magnitude [43], which depends on the use of different apparatus, the sample textures and preparation techniques, the lack of reference samples, the applied fluids and pressures, the local heterogeneities, the clay content, and so on. The most part of these influencing factors are much easier to take into account in the numerical experiment setup.

It’s well known that the procedure of grid refinement influences on the fluid and gas flow properties. This problem was investigated for hydrodynamic flow over wings [44] and for vortex flows [45]. Similar problem also exists for digital images with narrow pore throats which typically contain only few nodes between impermeable boundaries (near 10). Unfortunately, the results for samples with real porous structures are lacking. The dependence of LBE solution on the grid step was investigated for BCC and FCC models in [25,26], and for the model of random packing of spherical particles in [17]. The level of grid refinement didn’t exceed 5 in these studies.

As already noted in [31–34], the image resolution significantly affects the characteristics of digital models. The high-resolution model contains larger number of nodes. Also, the inevitable increase in the number of cells after grid refinement is expected. Thus, the most actual problem in the pore-scale modeling is the compromise between two interrelated indicators: the calculation accuracy, which depends on image resolution and grid refinement level, and the computational cost.

The motivation and objective of this paper is to perform numerical experiments in digital models of natural heterogeneous porous media. As samples of study, a series of X-ray CT images of natural sandstones is used. They have uniform pore structure presented mainly by large pores (1 μm and more). They are well resolved at submicron resolution and play an important role in heavy oil displacement. A special attention is paid to the sensitivity of NSE and LBE (with MRT collision operators) to the grid refinement level, and also answer to the question – whether a solution convergence or independence of grid step achieved, when using each mathematical model? In connection with this, we study the effect of grid coarsening which can significantly save computer and time resources in the case of satisfactory results.

2. Materials and methods

In our study, for pore-scale single-phase flow simulation, the stationary Navier-Stokes and the lattice Boltzmann equations are applied. In the LBE, the MRT collision operator is used. The LBE with the MRT model will be indicated as LBE(MRT).

2.1. LBE formulation

In the LBE, the fluid flow is considered as a dynamics of particles ensemble with given finite number of possible velocities. The flow domain in standard case is a grid with square or cubic cells. The set of these cells forms a lattice. During a time step Δt, the particles without interaction with each other can make one act of displacement between adjacent nodes. One-particle distribution functions $f(\mathbf{r}, \boldsymbol{u}, t)$ are used to describe the state of the system in each grid node. This function shows the part of particles at time t located in the vicinity of point $\mathbf{r}(x, y, z)$ with coordinates from x to $x+\Delta x$, from y to $y+\Delta y$, from z to $z+\Delta z$ and with velocity range from $\mathbf{u}(u_x, u_y, u_z)$ to $\mathbf{u}(u_x+\Delta u_x, u_y+\Delta u_y, u_z+\Delta u_z)$ [11].

In this paper, we consider three-dimensional case. Possible directions for particles displacement are described using D3Q19 model. The set of velocities $\mathbf{e}_i$ is given in [46]. Each velocity vector from set of $\mathbf{e}_i$ corresponds to the function $f_i(\mathbf{r}, t)$ which depends only on t and $\mathbf{r}$.

The dynamics of particles ensemble is described in several stages. The first is a streaming step. At this stage, during Δt the particles move to neighboring nodes in possible for D3Q19 directions. The second stage is a collision of particles, as a result of which the distribution function tends to the equilibrium state. Evolution of f_i in time and space is described by Eq. (1):

$$f_i(\mathbf{r} + \mathbf{e}_i\Delta t, t + \Delta t) = f_i(\mathbf{r}, t) + \Omega_i(\mathbf{r}, t) \tag{1}$$

$\Omega_i(\mathbf{r}, t)$ is a collision operator. The macroscopic density $\rho(\mathbf{r}, t)$ and velocity $\mathbf{u}(\mathbf{r}, t)$ of the fluid are calculated in each node using Eqs. (2) and (3):

$$\rho(\mathbf{r}, t) = \sum_{i=1}^{19} f_i(\mathbf{r}, t) \tag{2}$$

$$\mathbf{u}(\mathbf{r}, t) = \frac{1}{\rho}\sum_{i=1}^{19} \mathbf{e}_i f_i(\mathbf{r}, t) \tag{3}$$

When studying flow processes in the LBE, the Mach number should not exceed 0.1 [11]. The pressure P is associated with fluid density by following relation: $P = \rho c^2/3$, where $c = \Delta l/\Delta t$ – the lattice speed, Δl – the grid step.

The relaxation parameter τ controls the kinematic viscosity μ (Eq. (4)):

$$\mu = \left(\frac{2\tau - 1}{6}\right)\frac{\Delta l^2}{\Delta t} \tag{4}$$

Parameter τ can't take values less than 0.5 because negative values of fluid viscosity are not physical. As τ increases, the viscous properties of the fluid also grow. The time step Δt is a proportionality coefficient between τ and μ.

In the MRT model, unlike the SRT model, different fluid motion characteristics tend to equilibrium state at different rates. MRT collision operator is described by [19]:

$$\Omega_i = -M^{-1}S(m_i - m_i^{eq}) \tag{5}$$

In Eq. (5), $m_i = \sum_{k=1}^{19} M_{ik} \cdot f_k$. The view of matrix M and formulas for calculation of m_i^{eq} in D3Q19 model are given in [15,20,46]. The components of the diagonal matrix S in Eq. (5) are described in [25]. The set B for matrix S given in [25] ensures the independence of permeability coefficients from viscosity or τ.

2.2. Stationary Navier-Stokes and continuity equations

This model is represented by the following system of equations:

$$\mathrm{div}\mathbf{u} = 0 \tag{6}$$

$$\mu\Delta\mathbf{u} = \frac{1}{\rho}\nabla P \tag{7}$$

Inertial component $(\mathbf{u}, \nabla)\mathbf{u}$ in Navier-Stokes equations (7) is absent. This is due to typically low velocity of the fluid flow in pores (10^{-4}–10^{-6} (m/s)) and the higher order of smallness relative to the rest constituents of the Eq. (7) [7,8].

The pressure and velocity depend only on the cells coordinates. Eqs. (6) and (7) are solved by the finite differences method [6]. The grid is formed on the basis of the "markers and cells" (MAC) method [6–8]. In the MAC method, the pressure is determined in the center of cell, and the velocity components – in the center of its faces (Fig. 1). The matrix equation, obtained after finite-difference approximation [6], is solved using SPARSKIT library in Krylov subspace [40]. We used ILU matrix decomposition (preconditioner ILUT) and iterative solvers BCGSTAB and GMRES [40]. This set of procedures provides a successful solution convergence in all calculation variants.

2.3. Boundary and initial conditions in LBE and NSE

The pore space of flow domain, on which the computational experiments are carried out, is completely filled with fluid which has following properties: $\rho/(\mathrm{kg/m^3}) = 1000$, $\mu/(\mathrm{m^2/s}) = 1 \cdot 10^{-6}$. A fluid with the same properties is injected through the conventionally left side of the sample, perpendicular to the OX axis, and is selected through the conventionally right side. The fluid flows at constant pressure difference between input and output boundaries. Other external borders are impermeable.

For the NSE, the initial flow conditions are not implied because of its stationary. In the digital models of porous media, the impermeable boundary is located in a half-step from the centers of solid and pore cells (Fig. 1). On the cells belonging to the skeleton, the liquid adhesion and non-flow conditions are applied. According to them, the normal and tangential to the boundary velocity components are equal to zero. The detailed description is given in [6,7]. For the velocity component which is normal to the output boundary the Neumann condition is applied.

For the LBE, the distribution functions $f_i(\mathbf{r},0)$ at the initial time correspond to the equilibrium state calculated by Eq. (8) at $\mathbf{u} = 0$.

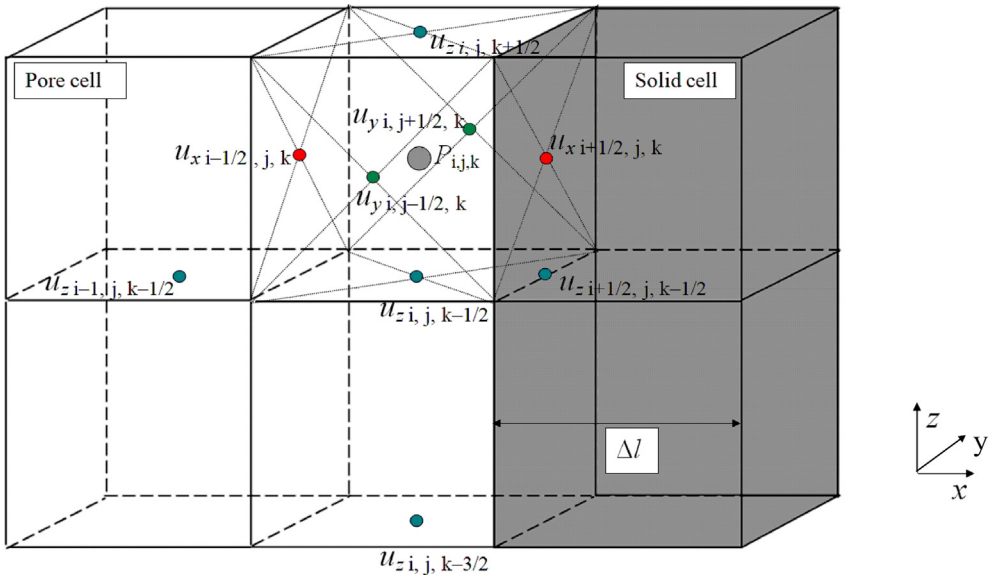

Fig. 1. Cell structure in the MAC method. Pressure is determined in the center of cell, and the velocity components – in the center of its faces.

$$f_i^{eq}(\rho,\mathbf{u}) = w_i\rho\cdot\left(1+3\frac{(\mathbf{e}_i\cdot\mathbf{u})}{c^2}+4.5\frac{(\mathbf{e}_i\cdot\mathbf{u})^2}{c^4}-1.5\frac{\mathbf{u}^2}{c^2}\right) \quad (8)$$

$w_1 = 1/3,\ w_{2-7} = 1/18,\ w_{8-19} = 1/36$ are the weight coefficients in D3Q19.

The boundary conditions on the input and output boundaries of the flow domain are given by Zou and He relations [47,48]. The grid which corresponds to the half-step location of impermeable boundary is a "mid-grid" in the LBE (Fig. 1). On the solid boundaries, the adhesion and non-flow conditions are realized using the "bounce-back" rule [13].

2.4. Image processing and sample description

The digital structure of the pore space was extracted using X-ray computed tomography. The scans of rocks were made on the micro-/nanofocus X-ray monitoring system for computed tomography and 2D inspection GE Phoenix v|tome|x s 240. All measurements were performed using a microfocus X-ray tube. For each sample, optimal values of the X-ray tube amperage and voltage, which ensure the best contrast of the image, were selected. 3D distribution of the linear coefficient of the X-ray radiation attenuation in the volume of investigated sample was computer reconstructed after two-dimensional shadow projections processing. Two-dimensional projections were obtained during scan procedure at various rotating angles of the sample ($0° < \varphi < 360°$).

Preliminary computer processing, segmentation and analysis of the digital cores geometric characteristics were made in Avizo Fire Edition software (Visualization Sciences Group). To divide the image into pores and skeleton, we used standard binarization option "Auto thresholding" in Avizo Fire. The study of segmentation algorithms and computer image processing is beyond the scope of this study. The affect of these procedures on the characteristics of digital models are described in [29–31].

In this paper, a series of oil-saturated sandstones from Ashalchinskoye (Tatarstan, Russia) and Vostochno-Birlinskoe (Ulyanovsk region, Russia) oil fields were used. The rock component of samples is polymineral and consists, in the main, of quartz, and also contains feldspars, dolomite, siderite, calcite, illite, kaolinite, clay minerals, and hematite. We selected a set of cubic cores with different sizes (from 3.0 to 6.0 mm) for which X-ray tomographic scanning with high resolution was performed. The resolutions of digital models are in the range from 2.9 to 5.9 μm. Also, for reproduction of our results by the other authors, we used a series of sandstones digital models from the open library of Imperial College London [49].

Fig. 2 shows the digital models fragments of Ashalchinskoye (Fig. 2a) and Vostochno-Birlinskoe (Fig. 2c) sandstones with sizes of $300 \times 300 \times 300$ voxels, and porous structures which were extracted after images binarization (Fig. 2b and d). The resolutions of models are 5.8 μm and 3.2 μm, respectively. The gray color scale in Fig. 2a and c characterizes the intensity of X-ray radiation attenuation by different areas of the samples: light gray regions are the granules of sandstone, and the dark gray areas are the pore space. The binarized image in our method is viewed as a text file with (x, y, z) coordinates and with a pointer for each cell. For example, "1" is for pore and "0" is for skeleton.

3. Results and discussion

The implementation of mathematical models was in the form of software codes in Microsoft Visual Studio development environment using Fortran programming language. The calculations were made on Intel Core i7 which contains 8 logical cores. All algorithms were parallelized using OpenMP technology.

3.1. Models validation

The validation of models was carried out on two tests. The first is the flow simulation in channel with rectangular cross section and external impermeable boundaries. It is considered that one of the cross section sizes (for example, OZ) exceeds by several orders of magnitude the other (for example, OY). For these conditions, the analytical dependence is known (Eq. (9)):

$$u_x^{Analytic}(y) = \frac{\Delta P}{2\rho\mu L}(R^2 - y^2) \quad (9)$$

In Eq. (9), R – hydraulic radius in OY direction, y – distance from the channel axis to impermeable boundary, L – channel length. The fluid model takes following values: $\mu/(m^2/s) = 1.0\cdot10^{-6}$, $\rho/(kg/m^3) = 1000$. The pressure drop $\Delta P/(Pa)$ between input and output sections was $1\cdot10^{-3}$. The grid step $\Delta l/(m) = 0.01$ and the

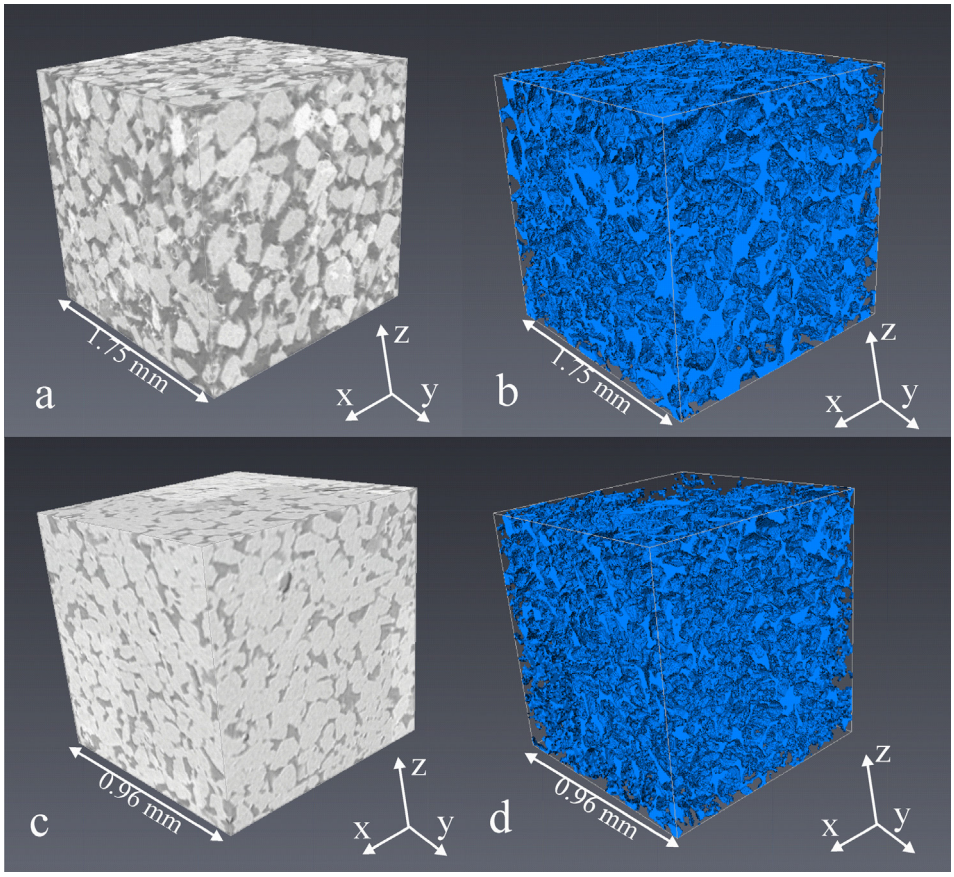

Fig. 2. Digital X-ray CT models with dimensions of 300 × 300 × 300 voxels: a – sandstone from Ashalchinskoye oil field, the resolution is 5.8 μm; b – pore space of sandstone from Ashalchinskoye oil field; c – sandstone from Vostochno-Birlinskoe oil field, the resolution is 3.2 μm; d – pore space of sandstone from Vostochno-Birlinskoe oil field.

time step for LBE is calculated by Eq. (4) for given value of the relaxation parameter τ.

A series of numerical calculations was performed for various numbers of nodes along OY direction using NSE and LBE(MRT). The grid dimension in OY direction was 7, 10, 15, 20, 30, 50 and 100 nodes. The number of nodes in OZ direction was 10^5. For estimation of the deviation Δ (in%) between numerical simulations and analytical solution (Eq. (9)), we used following formula: $\Delta = \frac{100}{N} \cdot \sum_{i=1}^{N} \frac{|u_x(y_i) - u_x^{Analityc}(y_i)|}{u_x^{Analityc}(y_i)}$, where N is a number of nodes in OY direction, u_x – the velocity distribution obtained by numerical simulations. Calculations using LBE(MRT) were carried out for τ = 0.51, 0.52, 0.55, 0.60, 0.70, 0.80, 1.0, 1.2 and 1.5. The results are presented in Fig. 3. Firstly, the solutions obtained with LBE(MRT) are practically independent of τ. Secondly, the solution dependence on the grid dimension for LBE(MRT) is observed. Thirdly, the results obtained with NSE have a higher accuracy order in comparison with LBE(MRT). Δ for NSE is about $10^{-4\%}$ and practically doesn't depend on the grid dimension.

As the second test, the permeability coefficients of the tubes with different areas of the square cross sections were calculated. The measurement of absolute permeability is carried out using Darcy's law at steady flow regime. The simulations were carried out for grid dimensions varied from 5 to 100 nodes. In further study, the permeability coefficients calculated using LBE(MRT) and NSE will be denoted as $k^{LBE(MRT)}$ and k^{NSE}, respectively. According to obtained results, $k^{LBE(MRT)}$ exceed k^{NSE} in all cases of cross-section sizes. The discrepancy between $k^{LBE(MRT)}$ and k^{NSE} decreases from 2.3% to 0.01% with increase in grid dimension from 5 to 100 nodes.

3.2. Permeability coefficients of the sandstones digital models, calculated using NSE and LBE(MRT)

In this section, the permeability coefficients of sandstones digital models from the open library of Imperial College London [49] are calculated. The numerical simulations were carried out on fragments with dimensions of 200 × 200 × 200 voxels. Image resolutions and their characteristics are shown in Table 1.

According to Table 1, $k^{LBE(MRT)}$ values exceed k^{NSE} for each sample. The relative error Δ shown in column 6 ($\Delta = 100 \cdot (k^{LBE(MRT)} - k^{NSE})/k^{NSE}$) is significant. Its level is about 20–30%.

Fig. 4 illustrates the field of u_x components in the pore space of Berea sandstone. This distribution was obtained for $\Delta P/(\text{Pa}) = 10$, $\mu/(\text{m}^2/\text{s}) = 1.0 \cdot 10^{-6}$ and $\rho/(\text{kg}/\text{m}^3) = 1000$. Fig. 4a shows the flow field in 3D space, obtained in solving the NSE (u_x^{NSE}); Fig. 4b and 4c demonstrate u_x^{NSE} velocity distribution in the slices №. 48 and №. 88 which are perpendicular to the flow direction (OX axis). A comparison of velocity fields, obtained with the NSE and the LBE (MRT) ($u_x^{LBE(MRT)}$), along the lines shown in Fig. 4b and 4c is illustrated in Fig. 4d and 4e, respectively. It can be concluded that u_x^{NSE} and $u_x^{LBE(MRT)}$ have similar distribution trends in the cross section of the pore channel, but the numerical values of $u_x^{LBE(MRT)}$ are significantly higher than u_x^{NSE}. As a result, $k^{LBE(MRT)}$ exceed k^{NSE} (Table 1).

So, we have found a significant discrepancy between NSE and LBE results. Therefore, the applying of the initial digital models for permeability coefficients calculation suggests uncertainty in using either NSE or LBE for obtaining the accurate characteristics.

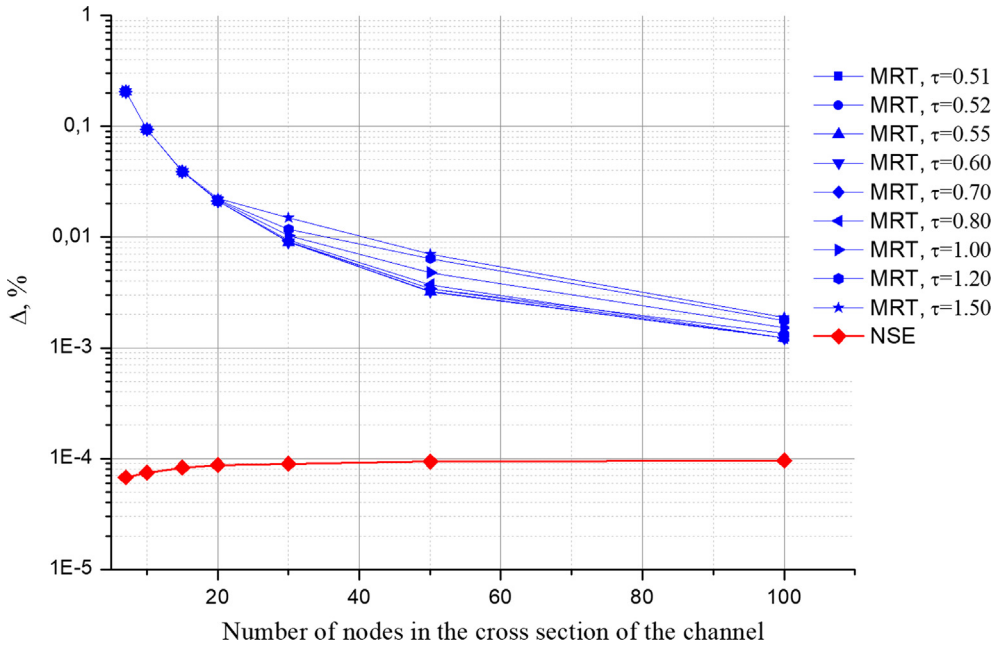

Fig. 3. The dependence of NSE and LBE(MRT) solutions on the number of nodes in cross-section of the channel. The relative error Δ was obtained in comparison with the analytical formula.

Table 1
The porosity and permeability coefficients of sandstones digital models, calculated using NSE and LBE(MRT).

Sample	Image resolution/(μm)	Porosity/(%)	$k^{LBE(MRT)}/(\mu m^2)$	$k^{NSE}/(\mu m^2)$	Δ/(%)
Berea Sandstone	3.2	0.192	0.484	0.36	34.4
Sandstone S1	8.68	0.141	3.01	2.36	27.5
Sandstone S2	4.95	0.245	5.75	4.638	24.0
Sandstone S3	9.1	0.171	1.45	1.131	28.2
Sandstone S4	8.96	0.166	0.612	0.5	22.4
Sandstone S5	4	0.193	3.88	3.201	21.2
Sandstone S6	5.1	0.198	10.13	8.56	18.3
Sandstone S7	4.8	0.237	5.48	4.44	23.4
Sandstone S8	4.89	0.311	12.7	10.62	19.6
Sandstone S9	3.4	0.213	1.98	1.644	20.4

3.3. Effect of grid refinement

In this section, we investigate the effect of grid refinement on single-phase flow characteristics. As the samples for study, the sandstones digital models from Ashalchinskoye oil field with resolution of 5.0 μm (sample A) and from Vostochno-Birlinskoe oil field with resolution of 3.0 μm (sample B) were used. The image slices perpendicular to the OZ axis are shown in Fig. 5a for sample A and in Fig. 5b for sample B. The square sections of 100 × 100 cells, which were cut from these slices, are illustrated in Fig. 5c and d. Blue color corresponds to the pore space. The sizes of pore channels in cell numbers shown in Fig. 5c and d vary from 3 to 15. The reasonableness of grid refinement is the small width of the pore channels which is typical for X-ray CT models. Therefore, the solution dependence on the refinement level is expected, but it is unclear how grid refinement will affect the permeability coefficients calculated using NSE and LBE(MRT).

The grid refinement was simultaneously made along each axis of coordinate system, as a result of which the grid step obviously changes also in all directions. The new cells obtained after refinement will be called subvoxels. The algorithm assumes uniform refinement: the subvoxels, which are the part of the initial cubic cell, also have the shape of a cube, the equal volume and size. The pore structures of digital models before and after refinement are similar. In this paper, the level of grid refinement (we denote as n^{ref}) is defined as the multiplicity of the grid step splitting. n^{ref} takes values from two to ten. So, for $n^{ref} = 2$, the cubic cell with volume V and size L is divided into 2^3 subvoxels with volumes of $V/8$ and sizes of $L/2$. For $n^{ref} = 10$, the number of nodes increases in 10^3 times.

For the numerical experiments, the cubic fragments with relatively small dimensions of 50 × 50 × 50 cells were selected from samples A and B. The limitation in the digital model size is due to the fact that for $n^{ref} = 10$, the number of subvoxels in flow domain is 500^3. So many nodes impose significant requirements on the computer equipment and time. A series of numerical experiments for $n^{ref} = 1, 2, 3, 4, 5, 6, 7, 8, 9$ and 10 were carried out. Calculations using LBE(MRT) were made only for $\tau = 0.8$ due to permeability independence of the relaxation parameter [25]. The results for samples A and B are shown in Fig. 6a and b, respectively.

Based on obtained curves, following regularities were revealed. Grid refinement plays a significant role for single-phase flow simulations and is manifested for each mathematical model. The grid refinement in 10 times reduces $k^{LBE(MRT)}$ by 42% for sample A and by 47% for sample B. When using the NSE, the grid refinement reduces k^{NSE} by 10% for sample A and by 12% for sample B. It should

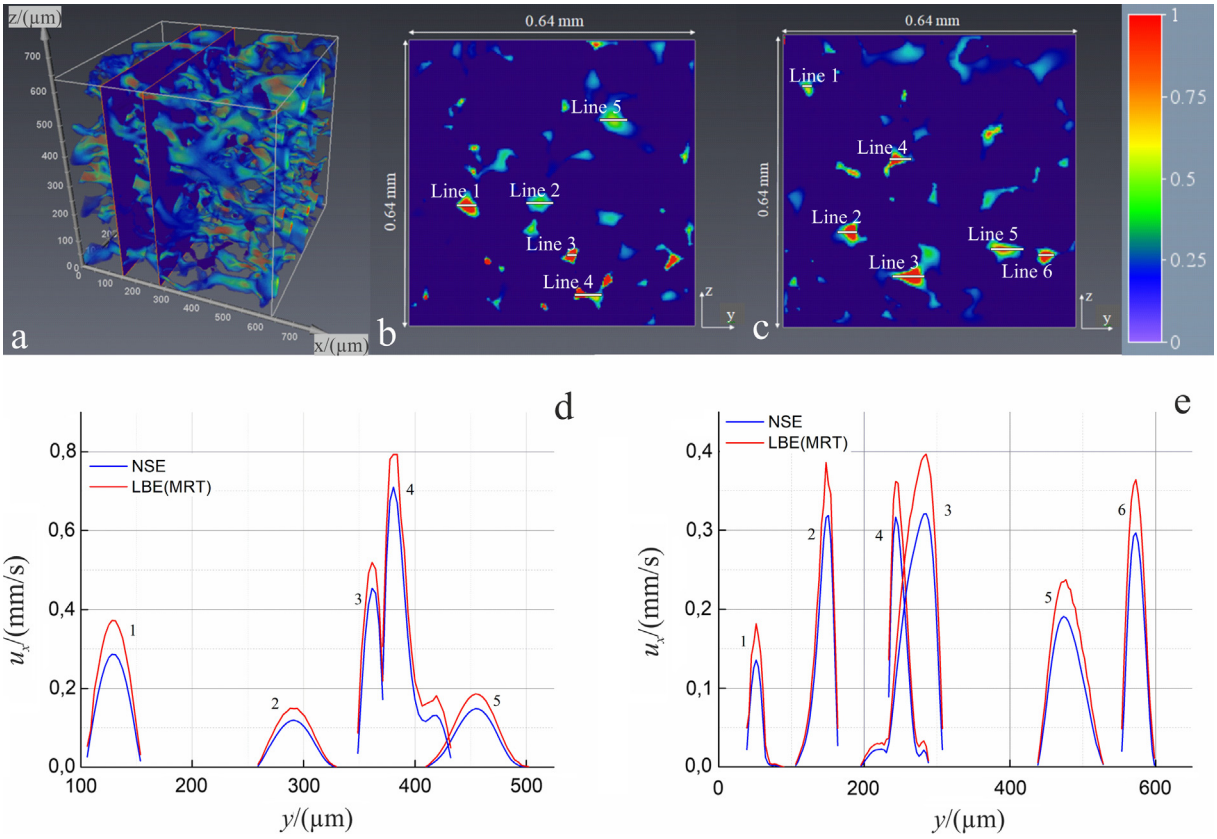

Fig. 4. Velocity field in the pore space of Berea sandstone: a – u_x^{NSE} in 3D; b, c – u_x^{NSE} in the slices № 48 and № 88 which are perpendicular to the flow direction; d, e – comparison between u_x^{NSE} and $u_x^{LBE(MRT)}$ along lines plotted in slices № 48 and № 88, respectively. The color scale is normalized to 1. Dimension and resolution of image is 200^3 voxels and 3.2 μm. (For interpretation of the references to colour in this figure legend, the reader is referred to the web version of this article.)

be noted that the discrepancy between $k^{LBE(MRT)}$ and k^{NSE} decreases with growth of the grid refinement level. For sample A, Δ varies from 24.6% to 2.86% and from 27.2% to 3.82% for sample B.

The dependence of relative deviation Δ (in%) on n^{ref} is calculated by: $\Delta(n^{ref}) = 100 \cdot (k(n^{ref}) - k(10))/k(10)$. $k(n^{ref})$ in last formula are the permeability coefficients $k^{LBE(MRT)}$ and k^{NSE} calculated at given n^{ref}, $k(10)$ are the permeability coefficients $k^{LBE(MRT)}$ and k^{NSE} calculated at $n^{ref} = 10$. From the point of solution convergence, it was found that increase in n^{ref} leads to decrease in dependence of the permeability coefficients on this parameter. If we assume that the solution is considered independent of n^{ref} at $|\Delta| < 1\%$, then for the NSE it is achieved at $n^{ref} \geqslant 3$ for samples A and B. For $n^{ref} = 9$, $\Delta \approx 0.01\%$ for the NSE. When using LBE(MRT), $|\Delta| < 1\%$ only at $n^{ref} = 9$ for each sample. Taking into account that Δ is calculated in comparison with permeability computed at $n^{ref} = 10$, it can be concluded that for LBE(MRT), in contrast to NSE, the tenfold refinement of grid step is insufficient for solution convergence. Therefore, the NSE, from a point of solution convergence, has an advantage over LBE, but, on the other hand, the requirements to effectiveness of numerical methods in the NSE are higher too [42].

It is known that the nonstationary Navier-Stokes and continuity equations can be obtained from the lattice Boltzmann equations up to small values using Chapman-Enskog expansion [11]. We demonstrate that these mathematical models have different sensitivity to the effect of grid refinement. Consequently, despite the implementation of the mass and moments conservation laws, the deviations of results obtained by two models are due to the different accuracy of the boundary conditions near impermeable cells. Indeed, the "bounce back" procedure in the LBE has the first order of accuracy [11], whereas the finite-difference approximations in the NSE – the second [6]. The various interpolation schemes of the "bounce back" condition considered in [25] insignificantly increase the accuracy. The faults of the boundary conditions are also reinforced by the fact that the deviation between NSE and LBE solutions decreases with growth of the grid refinement level.

The distribution of u_x in sample A is shown in Fig. 7. Fig. 7a–c illustrate the velocity fields u_x^{NSE} on one slice of the 3D model for $n^{ref} = 1$, 3 and 6, respectively. Obviously, the grid refinement improves visual detailing of the velocity field in pore space. In Fig. 7d and e, u_x^{NSE} and $u_x^{LBE(MRT)}$ fields along the line plotted in Fig. 7a–c are compared at $n^{ref} = 1$, 3, 5 and 10. According to graphs, the biggest difference between NSE and LBE(MRT) solutions is observed for $n^{ref} = 1$, whereas for $n^{ref} = 3$ the discrepancy significantly reduced. This effect is in agreement with results shown in Fig. 6a and b. The relative deviation between $k^{LBE(MRT)}$ and k^{NSE} at $n^{ref} = 1$ for samples A and B reaches 24.6% and 27.2%, respectively, and decreases to 10.7% and 12.3% for $n^{ref} = 3$.

The NSE solutions show that at $n^{ref} \geqslant 3$, the grid refinement affects the absolute permeability coefficients weakly (Fig. 6a and b). A small differences in u_x^{NSE} distributions for $n^{ref} = 3$ and 5 shown in Fig. 7d confirm this pattern. Curves $u_x^{LBE(MRT)}$ plotted in Fig. 7e for $n^{ref} \geqslant 3$ show weak, but, in comparison with NSE, stronger dependence on the refinement level. It should be noted that u_x^{NSE} distributions are not represented for $n^{ref} > 5$ because of their visual similarity with the curve plotted for $n^{ref} = 5$.

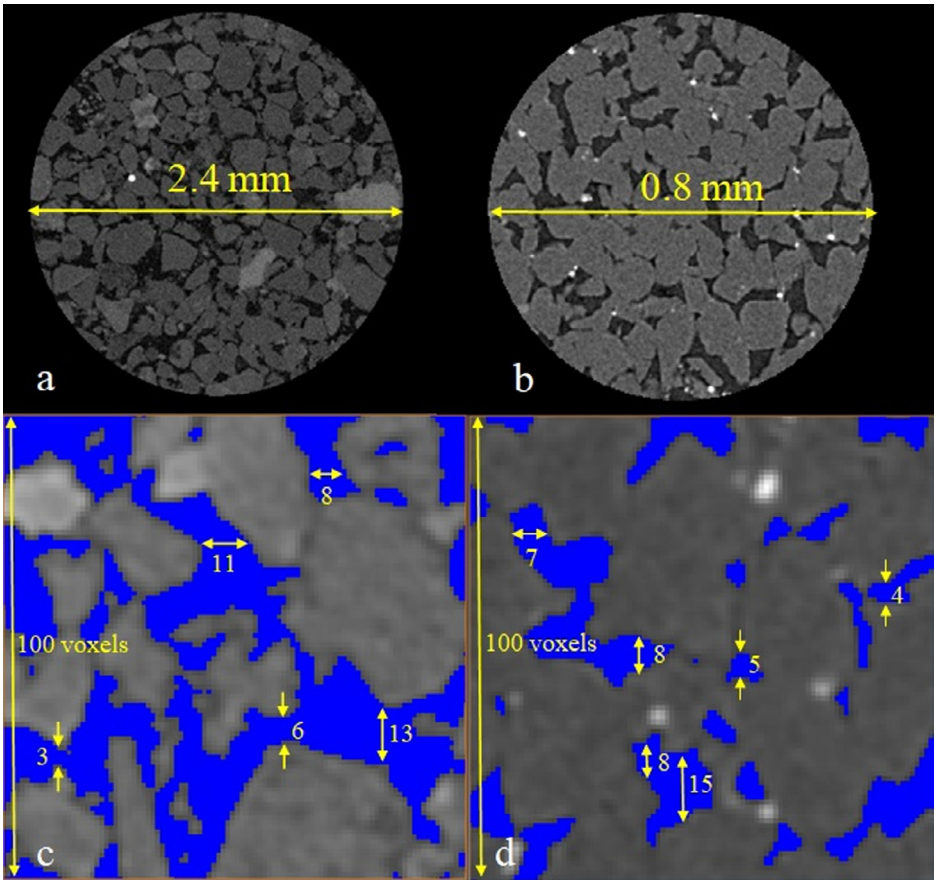

Fig. 5. Image slices of sandstone digital models: a – from Ashalchinskoye oil field (sample A); b – from Vostochno-Birlinskoe oil field (sample B); c, d – the fragments of image slices of samples A and B, respectively, their dimensions are 100 × 100 cells; blue color is a pore space, grey – skeleton. (For interpretation of the references to color in this figure legend, the reader is referred to the web version of this article.)

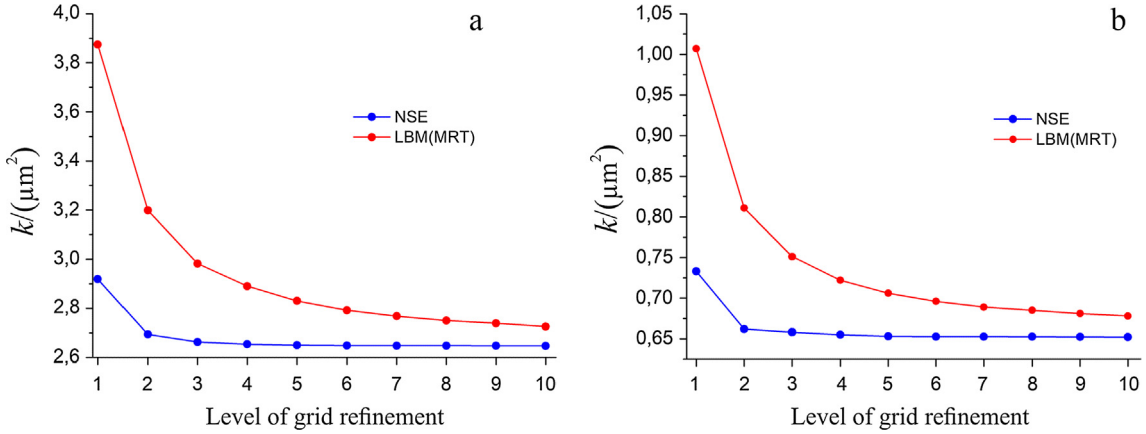

Fig. 6. Effect of grid refinement on the absolute permeability coefficients obtained using NSE and LBE(MRT): a – sample A; b – sample B.

3.4. Effect of grid coarsening

The results presented in Section 3.3 characterize strong dependence of the single-phase flow characteristics on the grid refinement. This modification, as earlier noted, leads to a multiple increase in the number of nodes. For the NSE, accurate results are obtained at $n^{ref} = 3$. When using LBE(MRT), the calculation error at least 5%, relatively grid independent values, can be achieved for $n^{ref} > 5$. Usually, numerical experiments on single- or two-phase flows in porous media are carried out on digital models with dimensions of $(200–300)^3$ cells [7,8,30]. After refinement of grid step into, for example, three and six times, the model with initial volume of 200^3 voxels will contain 600^3 and 1200^3 cells. Such dimensions, evidently, are too big for mathematical modeling. Since the grid refinement is an unavoidable procedure for obtaining of the accurate flow characteristics, the development of methods which modify the pore structure and reduce the grid dimension is needed. In this paper, we offer to produce the coarsening of model resolution. We accent that the resolution effect when X-ray CT scanning, as in [31–33], is not investigated

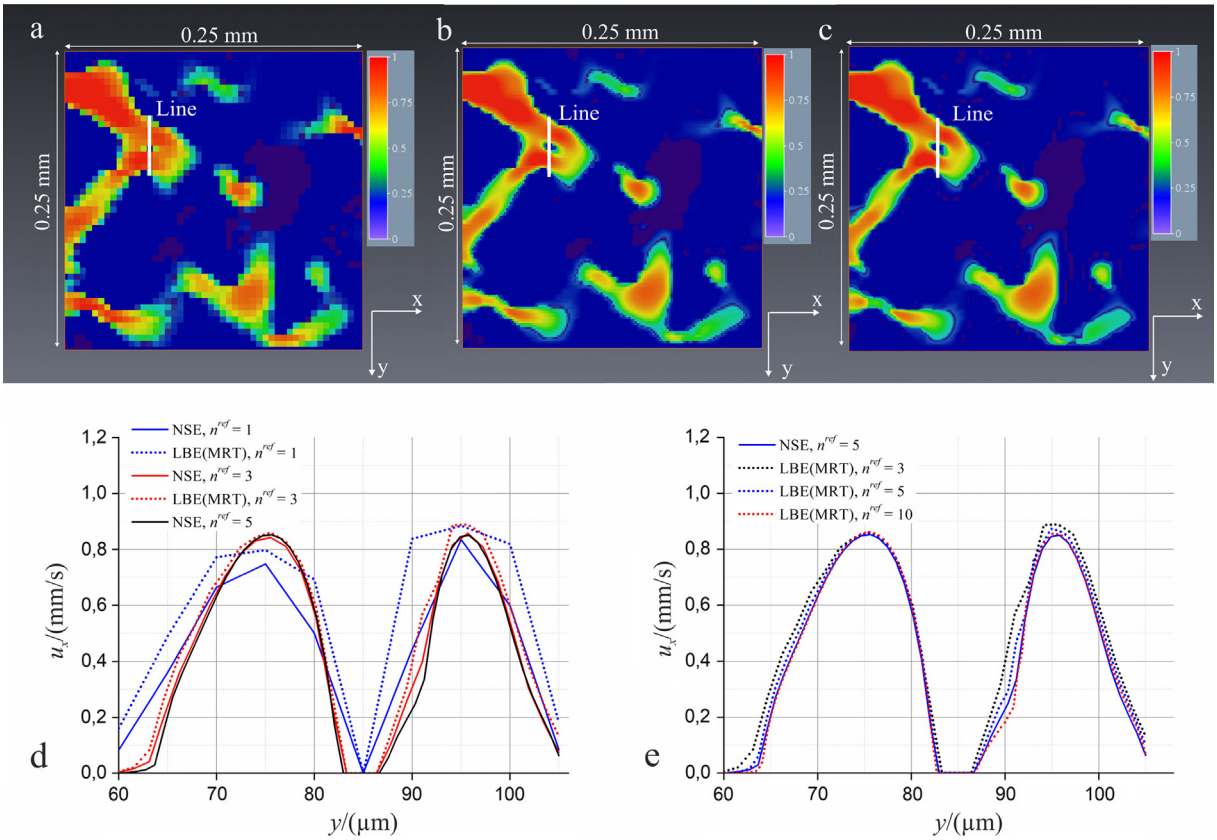

Fig. 7. The effect of grid refinement on u_x field in sample A, computed using NSE and LBE(MRT): a, b, c – u_x^{NSE} in the slice for n^{ref} = 1, 3 and 6 (the color scale is normalized to 1); d, e – the comparison of u_x^{NSE} and $u_x^{LBE(MRT)}$ along the line in slice for different n^{ref}. (For interpretation of the references to color in this figure legend, the reader is referred to the web version of this article.)

in our study. The image coarsening is artificial and produced using computer program. The algorithm of this procedure assumes the imposition of new grid with a bigger grid step on the initial digital model. If the volume of new large cell contains more than 50% pores, the new cell corresponds to the pore or, in the opposite case, to the skeleton. A similar technique was applied in [34].

The slices after grid coarsening in two and three times are shown in Fig. 8. The initial image was Berea sandstone with dimension of 198^3 voxels and with resolution of 3.2 μm. Thus, the resolutions of new models are 6.4 μm (Fig. 8b) and 9.6 μm (Fig. 8c), and their sizes are 99^3 and 66^3 cells, respectively.

The modification of porous media characteristics was investigated on 12 sandstones digital models with a wide range of the properties. The samples of Berea, S2, S8 and S9 sandstones from the Imperial College London open library [49] as well as the fragments of sandstones digital models from Ashalchinskoye and Vostochno-Birlinskoe oil fields were explored. The sizes of initial models were 102^3 voxels. For initial and coarsened models, the grid refinement level was in the range from 2 to 8. Single-phase flow was simulated using the LBE(MRT). The choice of the LBE is based on lower computational costs in our code implementation.

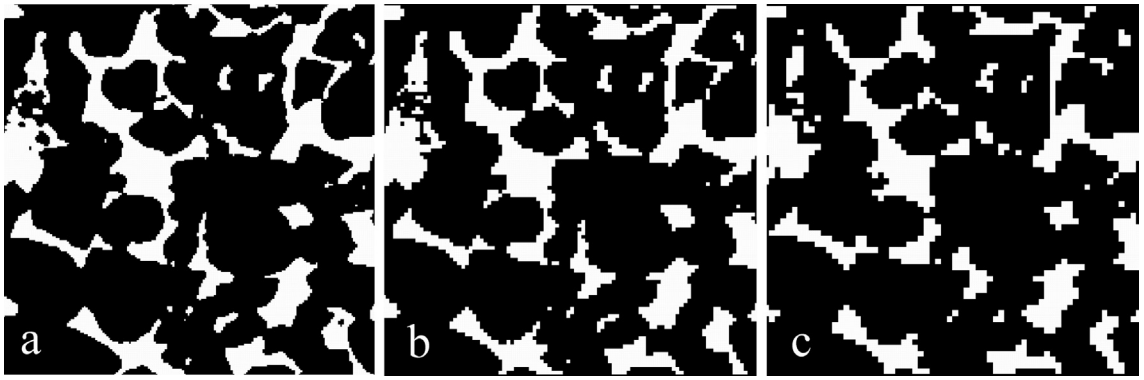

Fig. 8. Pore space modification of Berea sandstone after its coarsening: a – the initial image, the resolution is 3.2 μm; b – the model coarsened in two times, the resolution is 6.4 μm; c – the model coarsened in three times, the resolution is 9.6 μm. White is a pore space, black is a skeleton.

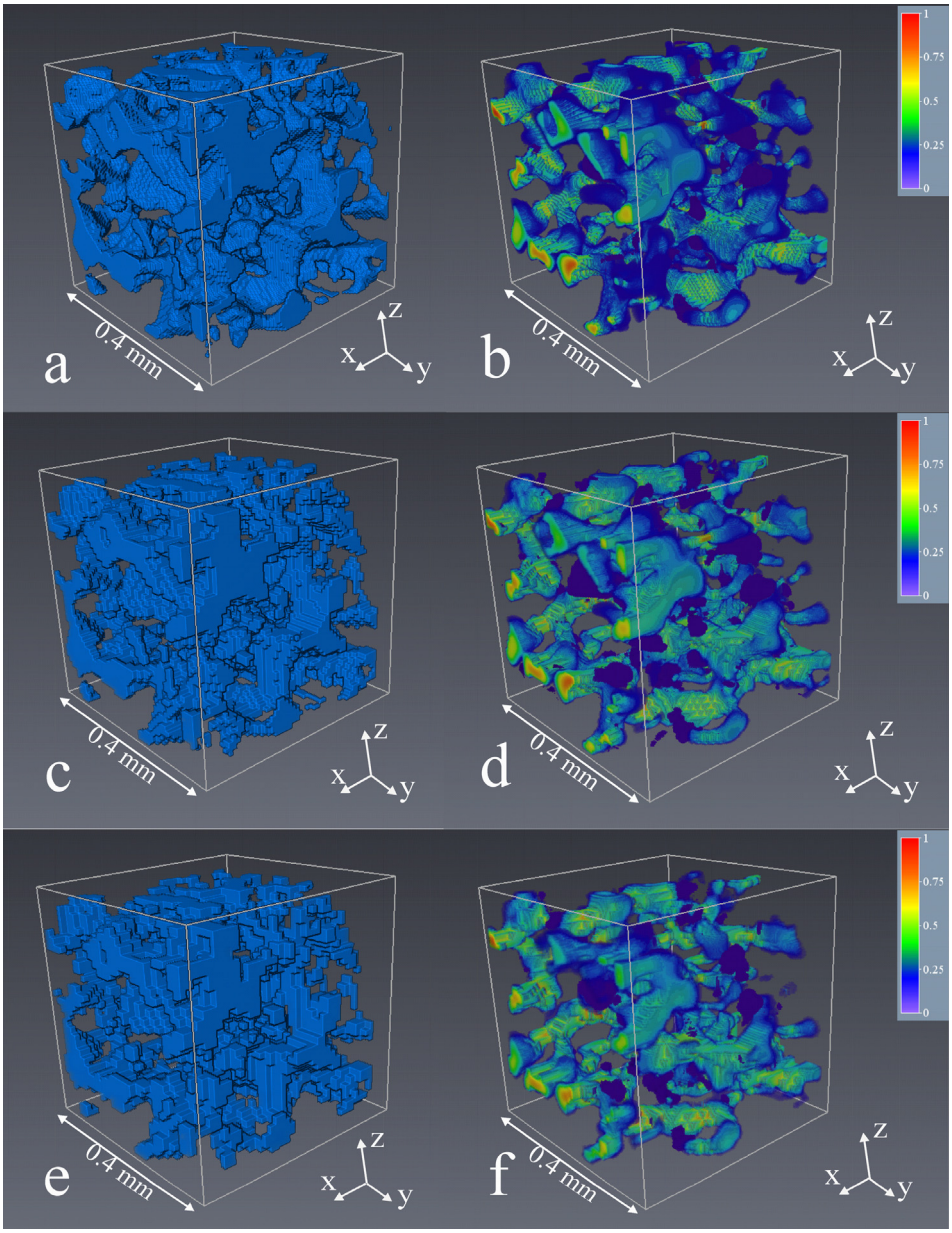

Fig. 9. Pore spaces and velocity fields in initial and coarsened models of sandstone from Vostochno-Birlinskoe oil field: a, c and e – pore spaces of initial, coarsened in two and three times models, respectively; b, d and f – velocity fields in initial, coarsened in two and three times models, respectively. The color scale for velocity is normalized to 1. Velocity field is illustrated for $n^{ref} = 4$. The dimension and resolution of initial model is 102^3 voxels and 4 μm. (For interpretation of the references to color in this figure legend, the reader is referred to the web version of this article.)

Fig. 9 illustrates the modified pore spaces of the sandstone from Vostochno-Birlinskoe oil field and the velocity distributions in initial and coarsened models. According to Fig. 9a, c and e, the modification of pore space is visible to the eye. The velocity distribution is shown for $n^{ref} = 4$ (Fig. 9b, d and f). Since the level of grid refinement was equal to four, it is hard to distinguish some graphical differences in velocity fields between coarsened and initial models.

The results of porosity and permeability calculations are presented in Table 2. The permeability coefficients in Table 2 were obtained at $n^{ref} = 8$; Δ in column 6 is defined as the relative deviation between permeability coefficients of coarsened and initial models. The range of flow properties is wide: [0.144–21.60] μm^2.

Based on obtained values, the porosities deviations of the modified models from initial images don't exceed 2% (column 4). The values in column 6 show that the differences in permeability coefficients between coarsened in two times models and initial images are in the limit of ±10%. This result was obtained for all of 12 test samples. Such magnitude of the deviation can be considered as successful, and images, which are coarsened in two times, therefore, can be used for the accurate flow simulations. When grid is coarsened in three times, the deviations of permeability coefficients exceed the limit of 10% for 10 samples (column 6). Therefore, despite the fact, that the grid coarsening is slightly affects the porosity (column 4) and, at the first glance, the velocity distribution (Fig. 9), the pore structures of the coarsened in three times models are not valid for accurate permeability calculations.

The values in column 7 characterize the ratio of the permeability k^1, calculated for initial model, and image resolution Δl.

Table 2
The porosity and permeability coefficients of the initial and coarsened models.

№	Name of sandstone	Resolution Δl/(μm)	Porosity/ (%)	Permeability/(μm^2)	Δ, %	$k^1/\Delta l$
1	Berea	3.2	0.192	0.144	–	0.045
		6.4	0.195	0.130	–9.72	
		9.6	0.190	0.0868	39.72	
2	Vostochno-Birlinskoe 3	3.32	0.173	0.265	–	0.080
		6.64	0.175	0.254	–4.15	
		9.96	0.167	0.183	30.94	
3	Vostochno-Birlinskoe 1	4.85	0.226	0.582	–	0.12
		9.70	0.230	0.591	1.54	
		14.55	0.218	0.339	41.75	
4	S9	3.34	0.166	0.751	–	0.225
		6.68	0.168	0.720	–4.12	
		10.02	0.164	0.560	25.43	
5	Ashalchinskoe 5	2.92	0.203	0.985	–	0.337
		5.84	0.205	1.066	8.22	
		8.76	0.200	0.692	29.74	
6	Vostochno-Birlinskoe 2	3.5	0.266	1.585	–	0.453
		7.0	0.271	1.681	6.05	
		10.5	0.261	1.262	20.37	
7	Ashalchinskoe 2	5.92	0.267	3.90	–	0.656
		11.84	0.270	4.154	6.11	
		17.76	0.264	3.283	20.96	
8	S2	4.95	0.228	4.845	–	0.979
		9.90	0.231	5.165	6.60	
		15.85	0.227	3.966	18.14	
9	Ashalchinskoe 4	5.8	0.339	9.420	–	1.624
		11.6	0.344	10.360	9.97	
		17.4	0.338	8.710	7.53	
10	Ashalchinskoe 3	5.8	0.358	14.80	–	2.555
		11.6	0.364	15.50	5.06	
		17.4	0.357	12.70	14.17	
11	Ashalchinskoe 1	2.9	0.289	8.320	–	2.847
		5.8	0.292	8.692	4.27	
		8.7	0.287	7.610	12.44	
12	S8	4.89	0.343	21.603	–	4.418
		9.78	0.348	23.260	7.67	
		14.64	0.345	21.040	2.60	

Comparing the values in column 6 and 7, it was revealed that increase in the magnitude of the flow properties leads to decrease in deviation between permeability coefficients of coarsened in three times and initial models. Such correlation for coarsened in two times models is absent.

4. Conclusions

This paper presents results of single-phase flow simulations in digital models of natural sandstones using the Navier-Stokes and the lattice Boltzmann equations with applying the MRT collision operators. For initial unmodified images, the strong differences between permeability coefficients calculated with use of the NSE and the LBE(MRT) were revealed. Therefore, the accuracy of simulation results in such models is low. The grid refinement significantly affects the permeability coefficients. The increase in the grid refinement level leads to decrease in the permeability coefficients. It was shown that LBE(MRT) solutions are more sensitive to the level of grid refinement than the NSE. For the test samples, the independence of the grid step for the NSE is achieved when the grid refinement level is 3, whereas for LBE(MRT), even a tenfold refinement is not enough for this. Also, the discrepancy between permeability coefficients, obtained with the NSE and LBE(MRT), decreases with increase in the grid refinement level. But, unfortunately, even when the level of refinement is 10, the relative deviation between permeability coefficients is significant and about 3–4%.

When investigating the grid coarsening, it was shown that permeability coefficients calculated on initial and coarsened in two times images differ in no more than 10%. The relative deviations of single-phase flow characteristic obtained on coarsened in three times images are out of this limit. It can be concluded that coarsened in two times models are valid for accurate single-phase flow simulations. This result allows to reduce the grid dimension in 2^3 times and to make a good economy in computational cost.

Conflicts of interest

The author declare that there is no conflict of interest.

Acknowledgements

The work is performed according to the Russian Government Program of Competitive Growth of Kazan Federal University and by Russian Foundation for Basic Research № 18-31-00134. Authors are thankful to Evgeny Statsenko for X-ray CT scanning.

References

[1] L. Zuo, S. Krevor, R.W. Falta, S.M. Benson, An experimental study of CO_2 exsolution and relative permeability measurements during CO_2 saturated water depressurization, Transport Porous Media 91 (2) (2012) 459–478, https://doi.org/10.1007/s11242-011-9854-2.
[2] A. Kumar, B. Maini, P. Bishnoi, M. Clarke, O. Zatsepina, S. Srinivasan, Experimental determination of permeability in the presence of hydrates and its effect on the dissociation characteristics of gas hydrates in porous media, J. Petrol. Sci. Eng. 70 (1) (2010) 114–122, https://doi.org/10.1016/j.petrol.2009.10.005.
[3] E. Charlaix, A. Kushnick, J. Stokes, Experimental study of dynamic permeability in porous media, Phys. Rev. Lett. 61 (14) (1988) 1595–1598, https://doi.org/10.1103/PhysRevLett. 61.1595.
[4] Sh.K. Gimatudinov, Physics of the Oil and Gas Reservoir, Nedra, Moscow, 1971, pp. 33–36.

[5] J. Dvorkin, N. Derzhi, E. Diaz, Q. Fang, Relevance of computational rock physics, Geophysics 76 (5) (2011) E141–E153, https://doi.org/10.1190/geo2010-0352.1.
[6] R.V. Vasilyev, K.M. Gerke, M.V. Karsanina, D.V. Korost, Solution of the Stokes equation in three dimensional geometry by the finite difference method, Math. Models Comput. Simul. 81 (1) (2016) 63–72, https://doi.org/10.1134/S2070048216010105.
[7] P. Mostaghimi, M.J. Blunt, B. Bijeljic, Computations of absolute permeability on micro-CT images, Math. Geosci. 45 (2013) 103–125, https://doi.org/10.1007/s11004-012-9431-4.
[8] T.R. Zakirov, A.A. Galeev, E.A. Korolev, E.O. Statsenko, Flow properties of sandstone and carbonate rocks by X-ray computed tomography, Curr. Sci. 110 (11) (2016) 2142–2147, https://doi.org/10.18520/cs/v110/i11/2142-2148.
[9] M. Piller, G. Schena, M. Nolich, S. Favretto, F. Radaelli, E. Rossi, Analysis of hydraulic permeability in porous media: from high resolution X-ray tomography to direct numerical simulation, Transp. Porous Media 80 (2009) 57–78, https://doi.org/10.1007/s11242-009-9338-9.
[10] S. Taheri, Sh. Ghomeshi, A. Kantzas, Permeability calculations in unconsolidated homogeneous sands, Powder Technol. 321 (2017) 380–389, https://doi.org/10.1016/j.powtec.2017.08.014.
[11] S. Succi, The Lattice Boltzmann Equation for Fluid Dynamics and Beyond, Oxford University Press, UK, 2001, p. 290.
[12] S. Chen, G. Doolen, Lattice Boltzmann method for fluid flows, Annu. Rev. Fluid Mech. 30 (1998) 329–364, https://doi.org/10.1146/annurev.fluid.30.1.329.
[13] I.C. Kim, Second order bounce back boundary condition for the Latice Boltzmann fluid simulation, KSME Int. J. 14 (1) (2000) 84–92, https://doi.org/10.1007/BF03184774.
[14] P. Yang, Z. Wen, R. Dou, X. Liu, Permeability in multi-sized structures of random packed porous media using three-dimensional lattice Boltzmann method, Int. J. Heat Mass Transf. 106 (3) (2017) 1368–1375, https://doi.org/10.1016/j.ijheatmasstransfer.2016.10.12 4.
[15] L. Hao, P. Cheng, Lattice Boltzmann simulations of anisotropic permeabilities in carbon paper gas diffusion layers, J. Power Sources 186 (2009) 104–114, https://doi.org/10.1016/j.jpowsour.2008.09.086.
[16] H. Sun, S. Vega, G. Tao, Analysis of heterogeneity and permeability anisotropy in carbonate rock samples using digital rock physics, J. Petrol. Sci. Eng. 156 (2017) 419–429, https://doi.org/10.1016/j.petrol.2017.06.002.
[17] V. Shabro, C. Torres, V.F. Javadpour, K. Sepehrnoor, Finite-difference approximation for fluid-flow simulation and calculation of permeability in porous media, Transport Porous Media 94 (2012) 775–793, https://doi.org/10.1007/s11242-012-0024-y.
[18] A.T. Borujeni, N.M. Lane, K. Thompson, M. Tyagi, Effects of image resolution and numerical resolution on computed permeability of consolidated packing using LB and FEM pore-scale simulations, Comput. Fluids 88 (2013) 753–763, https://doi.org/10.1016/j.compfluid.2013.05.019.
[19] E. Aslan, I. Taymaz, A.C. Benim, Investigation of the lattice Boltzmann SRT and MRT stability for lid driven cavity flow, Int. J. Mater. Mech. Manufact. 2 (4) (2014) 317–324, https://doi.org/10.7763/IJMMM.2014.V2.149.
[20] X. Niu, T. Munekata, Sh. Hyodoa, K. Suga, An investigation of water-gas transport processes in the gas-diffusion-layer of a PEM fuel cell by a multiphase multiple-relaxation-time lattice Boltzmann model, J. Power Sources 172 (2007) 542–552, https://doi.org/10.1016/j.jpowsour.2007.05.081.
[21] Y. Hu, D. Li, Sh. Shu, X. Niu, A multiple-relaxation-time lattice Boltzmann model for the flow and heat transfer in a hydrodynamically and thermally anisotropic porous medium, Int. J. Heat Mass Transf. 104 (1) (2017) 544–558, https://doi.org/10.1016/j.ijheatmasstransfer.2016.08.008.
[22] L.S. Luo, W. Liao, X. Chen, Y. Peng, W. Zhang, Numerics of the lattice Boltzmann method: effects of collision models on the lattice Boltzmann simulations, Phys. Rev. E 83 (2011), https://doi.org/10.1103/PhysRevE.83.056710 056710.
[23] P. Lallemand, L.S. Luo, Theory of the lattice Boltzmann method: dispersion, dissipation, isotropy, Galilean invariance, and stability, Phys. Rev. E 60 (2000) 6546–6562, https://doi.org/10.1103/PhysRevE.61.6546.
[24] R. Du, B. Shi, X. Chen, Multi-relaxation-time lattice Boltzmann model for incompressible flow, Phys. Lett. A 359 (2006) 564–572, https://doi.org/10.1016/j.physleta.2006.07.074.
[25] C. Pan, L.S. Luo, C.T. Miller, An evaluation of lattice Boltzmann schemes for porous medium flow simulation, Comput. Fluids 35 (2006) 898–909, https://doi.org/10.1016/j.compfluid.2005.03.008.
[26] A. Eshghinejadfard, L. Daróczy, G. Janiga, D. Thévenin, Calculation of the permeability in porous media using the lattice Boltzmann method, Int. J. Heat Fluid Flow 62 (2016) 93–103, https://doi.org/10.1016/j.ijheatfluidflow.2016.05.010.
[27] M.J. Blunt, B. Bijeljic, H. Dong, O. Gharbi, S. Iglauer, P. Mostaghimi, A. Paluszny, C. Pentland, Pore-scale imaging and modeling, Adv. Water Resour. 51 (2013) 197–216, https://doi.org/10.1016/j.advwatres.2012.03.003.
[28] Q. Xiong, T.G. Baychev, A.P. Jivkov, Review of pore network modelling of porous media: experimental characterisations, network constructions and applications to reactive transport, J. Contam. Hydrol. 192 (2016) 101–117, https://doi.org/10.1016/j.jconhyd.2016.07.002.
[29] P. Iassonov, T. Gebrenegus, M. Tuller, Segmentation of X-ray computed tomography images of porous materials: a crucial step for characterization and quantitative analysis of pore structures, Water Resour. Res. 45 (9) (2009) 1–12, https://doi.org/10.1029/2009WR008087.
[30] L. Leu, S. Berg, F. Enzmann, R.T. Armstrong, M. Kersten, Fast X-ray micro-tomography of multiphase flow in berea sandstone: a sensitivity study on image processing, Transp. Porous Media 105 (2014) 451–469, https://doi.org/10.1007/s11242-014-0378-4.
[31] N. Saxena, R. Hofmann, F.O. Alpak, J. Dietderich, S. Hunter, R.J. Day-Stirrat, Effect of image segmentation voxel size on micro-CT computed effective transport elastic properties, Mar. Pet. Geol. 86 (2017) 972–990, https://doi.org/10.1016/j.marpetgeo.2017.07.004.
[32] S. Peng, Q. Hu, S. Dultz, M. Zhang, Using X-ray computed tomography in pore structure characterization for a Berea sandstone: resolution effect, J. Hydrol. 472–473 (2012) 254–261, https://doi.org/10.1016/j.jhydrol.2012.09.034.
[33] S. Peng, F. Marone, S. Dultz, Resolution effect in X-ray microcomputed tomography imaging and small pore's contribution to permeability for a Berea sandstone, J. Hydrol. 510 (2014) 403–411, https://doi.org/10.1016/j.jhydrol.2013.12.028.
[34] S.M. Shah, F. Gray, J.P. Crawshaw, E.S. Boek, Micro-computed tomography pore-scale study of flow in porous media: effect of voxel resolution, Adv. Water Resour. 95 (2016) 276–287, https://doi.org/10.1016/j.advwatres.2015.07.012.
[35] F.O. Alpak, F. Gray, N. Saxena, J. Dietderich, R. Hofmann, S. Berg, A distributed parallel multiple-relaxation-time lattice Boltzmann method on general-purpose graphics processing units for the rapid and scalable computation of absolute permeability from high-resolution 3D micro-CT images, Comput. Geosci. (2018) 1–18, https://doi.org/10.1007/s10596-018-9727-7.
[36] A. Banari, C. Janßen, S.T. Grilli, M. Krafczyk, Efficient GPGPU implementation of a lattice Boltzmann model for multiphase flows with high density ratios, Comput. Fluids 93 (2014) 1–17, https://doi.org/10.1016/j.compfluid.2014.01.004.
[37] F. Kuznik, C. Obrecht, G. Rusaouen, J.J. Roux, LBM based flow simulation using GPU computing processor, Comput. Math. Appl. 59 (2010) 2380–2392, https://doi.org/10.1016/j.camwa.2009.08.052.
[38] P. Hénon, P. Ramet, J. Roman, PASTIX: a high-performance parallel direct solver for sparse symmetric positive definite systems, Parallel Comput. (2002) 301–321, https://doi.org/10.1016/S0167-8191(01)00141-7.
[39] J. Hogg, J. Scott, New parallel sparse direct solvers for multicore architectures, Algorithms 6 (2013) 702–725, https://doi.org/10.3390/a6040702.
[40] Y. Saad, Iterative methods for sparse linear systems, SIAM 528 (2003) p, https://doi.org/10.1137/1.9780898718003.
[41] U. Trottenberg, C. Oosterlee, A. Schüller, Multigrid, Academic Press, London, 2001, p. 631.
[42] D. Demidov, R. Rossi, Subdomain Deflation and Algebraic Multigrid: Combining Multiscale with Multilevel, arXiv preprint, 2017, arXiv: 1710.03940.
[43] J.T. Comisky, K.E. Newsham, J.A. Rushinget, T.A. Blasingame, A comparative study of capillary-pressure-based empirical models for estimating absolute permeability in tight gas reservoirs, Soc. Petrol. Eng. SPE-110050-MS (2007), https://doi.org/10.2118/110050-MS.
[44] J. Wackers, G. Deng, E. Guilmineau, A. Leroyer, P. Queutey, M. Visonneau, A. Palmieri, A. Liverani, Can adaptive grid refinement produce grid-independent solutions for incompressible flows?, J Comput. Phys. 344 (2017) 364–380, https://doi.org/10.1016/j.jcp.2017.04.077.
[45] S.M. Guzik, T.H. Weisgraber, P. Colella, B.J. Alder, Interpolation methods and the accuracy of lattice-Boltzmann mesh refinement, J. Comput. Phys. 259 (2014) 461–487, https://doi.org/10.1016/j.jcp.2013.11.037.
[46] S. Leclaire, A. Parmigiani, O. Malaspinas, B. Chopard, J. Latt, Generalized three-dimensional lattice Boltzmann color-gradient method for immiscible two-phase pore-scale imbibition and drainage in porous media, Phys. Rev. E 95 (2017), https://doi.org/10.1103/PhysRevE.95.033306 033306.
[47] Q. Zou, X. He, On pressure and velocity boundary conditions for the lattice Boltzmann BGK model, Phys. Fluids 9 (1997) 1591–1598, https://doi.org/10.1063/1.869307.
[48] M. Hecht, J. Harting, Implementation of on-site velocity boundary conditions for D3Q19 lattice Boltzmann simulations, J. Stat. Mech. P01018 (2010), https://doi.org/10.1088/1742-5468/2010/01/P01018.
[49] <http://www.imperial.ac.uk/earth-science/research/research-groups/perm/research/pore-scale-modelling/micro-ct-images-and-networks/>.